

# Digital Single Lens Reflex Camera Identification From Traces of Sensor Dust

Ahmet Emir Dirik, Husrev Taha Sencar, and Nasir Memon

**Abstract**—Digital single lens reflex cameras suffer from a well-known sensor dust problem due to interchangeable lenses that they deploy. The dust particles that settle in front of the imaging sensor create a persistent pattern in all captured images. In this paper, we propose a novel source camera identification method based on detection and matching of these dust-spot characteristics. Dust spots in the image are detected based on a (Gaussian) intensity loss model and shape properties. To prevent false detections, lens parameter-dependent characteristics of dust spots are also taken into consideration. Experimental results show that the proposed detection scheme can be used in identification of the source digital single lens reflex camera at low false positive rates, even under heavy compression and downsampling.

**Index Terms**—Digital forensics, digital single lens reflex (DSLR), sensor dust.

## I. INTRODUCTION

GIVEN the fast and widespread penetration of multimedia into all areas of life, the need for mechanisms to ensure reliability of multimedia information has become important. Today, digital media is relied upon as the primary way to present news, sports, entertainment, and information regularly that captures current events as they occur. They are introduced as evidence in court proceedings and commonly used in processing, analysis, and archiving of financial and medical documents. The long-term viability of these benefits requires the ability to provide certain guarantees about the origin, veracity, and nature of the digital media. For instance, the ability to establish a link between a camera and the digital image is invaluable in deciding the authenticity and admissibility of a digital image as legal evidence. Similarly, doctoring images is becoming more frequent as a way to influence people and alter their attitudes in response to various events [1], [2]. Hence, for conventional and online media outlets, the capability to detect doctored images before they are published is important to maintain credibility. Recent research efforts in the field of media forensics have begun to address these issues [3]–[5].

Manuscript received June 30, 2008; revised April 15, 2008. First published July 9, 2008; last published August 13, 2008 (projected). This work was supported by the National Institute of Justice under Grant 2006-92251-NY-IJ. The associate editor coordinating the review of this manuscript and approving it for publication was Dr. Jessica J. Fridrich.

A. E. Dirik is with the Department of Electrical and Computer Engineering, Polytechnic University, Brooklyn, NY 11201 USA (e-mail: emir@isis.poly.edu).

H. T. Sencar and N. Memon are with the Information Systems and Internet Security Laboratory, Polytechnic University, Brooklyn, NY 11201 USA.

Color versions of one or more of the figures in this paper are available online at <http://ieeexplore.ieee.org>.

Digital Object Identifier 10.1109/TIFS.2008.926987

A key problem in media forensics is the identification and analysis of media characteristics that relate to the acquisition device. These characteristics are essentially a combination of two interrelated factors: 1) the class properties that are common among all devices of a brand and model and 2) the individual properties that set a device apart from another in its class. Hence, research efforts have focused on the design of techniques to identify class and individual characteristics of data-acquisition devices without requiring a specific configuration of source devices [6], [7].

Two principal research approaches have emerged in the effort to establish characteristics that can link an image or video to its source. The first approach focuses on determining the differences in processing techniques and component technologies. For example, optical distortions due to a type of lens, the size of the imaging sensor, the choice of color filter array and corresponding demosaicing algorithm, and color-processing algorithms can be detected and quantitatively characterized by appropriate image-analysis techniques [3], [8]–[12]. The main difficulty with this approach is that many device models and brands use components by a few manufacturers and processing methods remain the same, or very similar, among different models of a brand. Hence, reliable identification of class characteristics of a device requires consideration of many different factors.

In the second approach, the primary goal is to identify unique characteristics of the source-acquisition device. These may be in the form of hardware and component imperfections, defects, or faults which might arise due to inhomogeneity in the manufacturing process, manufacturing tolerances, environmental effects, and operating conditions. The ability to reliably extract these characteristics makes it possible to match an image or video to its potential source and cluster data from the same source device together. The main challenge in this research direction is that reliable measurement of these minute differences from a single image is difficult and can be easily eclipsed by the image content itself. Another challenge is that these artifacts tend to vary in time and depend on operating conditions; therefore, they may not always yield positive identification. To date, proposed methods in this area depend primarily on faulty elements of the imaging device [13] and noise characteristics of the imaging sensor [12], [14]–[18].

In this paper, we present a new approach to source camera identification considering digital single-lens reflex (DSLR) cameras. The basis of our method is the appearance of dust spots or blemishes in DSLR camera images. Based on our earlier work [19], we demonstrate how these artifacts can be utilized as a fingerprint of the camera. DSLR cameras differ from digital compact cameras in various aspects: larger and

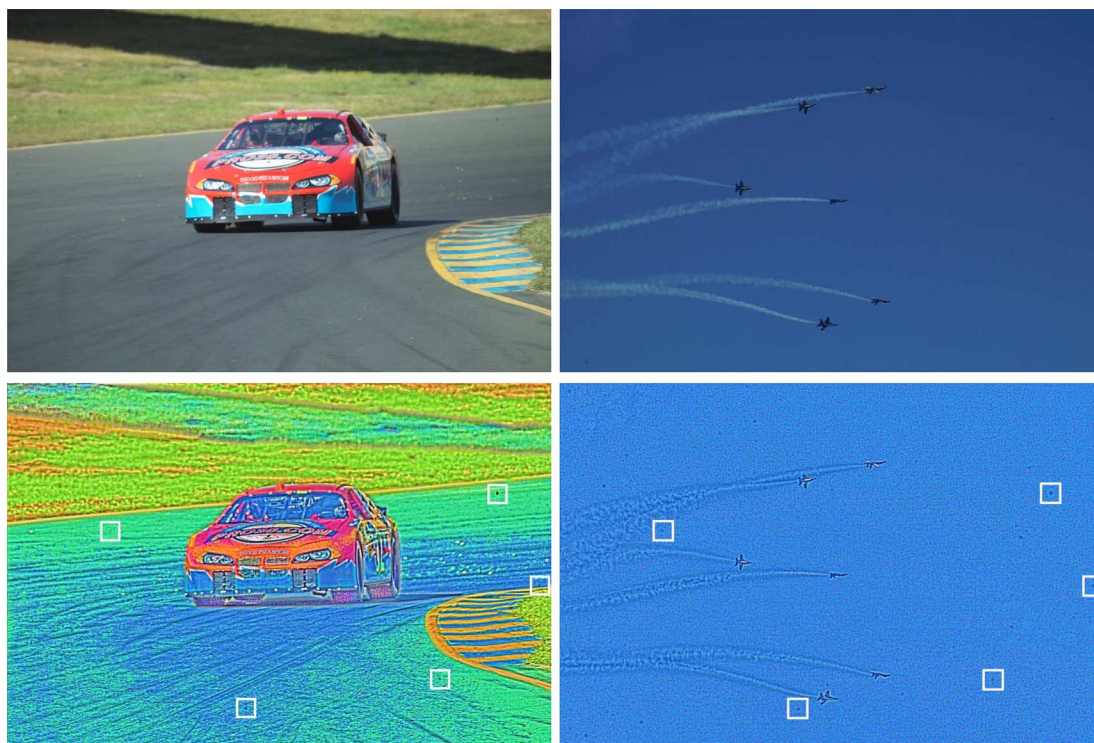


Fig. 1. Sensor dust appears in two different images taken with the same DSLR camera. Local histogram adjustment is performed to make dust spots visible (2nd row). White boxes show dust-spot positions.



Fig. 2. Dust spots may stay in the same position for years.

higher quality sensors with low noise power, parallax-free optical viewfinder that allows error-free viewing of the scenery, less shutter lag, interchangeable lenses, and a better control over depth of field. According to the 2006 International Data Corporation (IDC) report on the digital camera market, DSLR cameras showed a consistent growth with a total market and a 39% increase from the 2005 figure.<sup>1</sup> Not surprisingly, DSLR cameras also take the top place in most popular camera lists of

<sup>1</sup>[Online]. Available: [www.imaging-resource.com/NEWS/1175724860.html](http://www.imaging-resource.com/NEWS/1175724860.html).

photo sharing websites. For instance, the top five cameras for November 2007 in Flickr (flickr.com) and Pbase (pbase.com) photo sharing websites are all DSLR cameras.

The very nature of a DSLR camera allows users to work with multiple lenses, but this desirable feature creates a unique and undesired problem. Essentially, during the process of mounting/unmounting the interchangeable lens, the inner body and workings of the camera is exposed to the outside environment. When the lens is detached, very small dust particles are attracted to the camera and settle on the protective element (dichroic mirror or low-pass filter) in front of the sensor surface. These tiny specks of dust, lint, or hair cling to the surface and form a dust pattern which later reveals itself on captured images as blemishes or blotches. We will refer to this type of artifact as dust spots in the rest of this paper. Dust spots on two different images,<sup>2</sup> taken with same DSLR are given in Fig. 1. To make dust spots more visible, each pixel color is changed through histogram equalization in windows of small size. Dust spots become visible at low aperture rates (e.g., for high  $f$ -numbers) since a large aperture will allow light to wrap around the dust particles and make them out of focus. Moreover, sensor dust is persistent and accumulative and unless it is cleaned, it may remain in the same position for a very long time, as exemplified by images<sup>3</sup> in Fig. 2.

To deal with the sensor dust problem, various solutions have been proposed. Some DSLR camera manufacturers have already incorporated built-in mechanisms for dust removal. For example, Sony's Alpha A10 DSLR uses an antistat coating on

<sup>2</sup>[Online]. Available: [www.pbase.com/chucklantz/image/38843803](http://www.pbase.com/chucklantz/image/38843803) and [ldots /72922162](http://www.pbase.com/chucklantz/image/72922162).

<sup>3</sup>[Online]. Available: [www.pbase.com/chucklantz/image/47472873](http://www.pbase.com/chucklantz/image/47472873) and [ldots /image/72922162](http://www.pbase.com/chucklantz/image/72922162).

the CCD with a vibrating mechanism which removes the dust by shaking it. Similar vibration mechanisms are also utilized in Olympus E-300 and Canon EOS Rebel DSLR cameras. Nikon D50 and Canon Digital Rebel also offers a software solution to remove dust spots by creating a dust template of the camera.

A comprehensive benchmark on the performance of built-in dust removal mechanisms has been performed by [pixinfo.com](http://pixinfo.com).<sup>4</sup> The study involved four of the state-of-the-art DSLR cameras, namely, Canon EOS-400D, Olympus E-300, Pentax K10D, and Sony Alpha DSLR-A10. In the experiments, these four cameras were initially exposed to the same dusty environment, and later the cameras' built-in functions were used to remove these dust particles. Their results show that even after 25 consecutive invocation of the cleaning mechanism, dust spots were still present and their performance was far from satisfactory.<sup>5</sup>

Although vibration-based internal cleaning mechanisms do not work satisfactorily, they might influence the positions of dust particles over the filter component. This phenomenon can also be observable from the benchmarks mentioned before. To quantify the effect of internal cleaning mechanisms on dust-spot positions, the proposed dust detection algorithm was applied to two blank images taken with Canon EOS-400D after 2nd and 25th cleaning operations. These two images were obtained from the cleaning benchmark experiments in [pixinfo.com](http://pixinfo.com). Once dust positions are detected, they were compared with each other. After the 25th cleaning, %97.01 (24 dust particles) out of 803 dust particles remain in the same position. The maximum detected position shift after the 25th cleaning is 5.83 pixels (image size is  $[800 \times 532]$ ). Since dust shifts due to internal cleaning mechanisms are not significant, we will omit the effect of filter vibrations on dust positions in the rest of this paper.

An alternative solution is the manual cleaning of the dust by using chemicals, brushes, air blowing, and dust adhesive. Although these are known to be more effective, manual cleaning is a tedious task and may potentially harm the imaging sensor; therefore, it is not recommended by camera manufacturers.<sup>6</sup>

In this paper, we exploit this persistent nature of the sensor dust to match DSLR images to their sources. The matching can be realized by obtaining a dust pattern directly from the camera or from a number of images taken by the camera, as in Fig. 1. It should be noted that since the sensor dust problem is solely intrinsic to DSLR cameras, the detection of any sensor dust in a given image can be taken as strong evidence that the image source is a DSLR camera. In addition, by detecting traces of sensor dust, it may be possible to order images, taken at different times, in capturing time by evaluating accumulation characteristics of dust.

The rest of this paper is organized as follows. In Section II, we investigate the optical characteristics of sensor dust as a function of imaging parameters. In Section III, a model-based dust-spot detection method and its use in source camera identification is explained in detail. The efficacy of the proposed method is substantiated by experimental results for two different cases in

Section IV. The robustness of the proposed scheme to compression and downsampling is explained in Section IV. Finally, our conclusions are presented in Section V.

#### A. Related Work

The first work in the field of source identification was undertaken by Kurosawa *et al.* [14] for camcorders. Their method relies on the fact that each digital camcorder CCD sensor has a unique and intrinsic dark current noise pattern. This specific noise pattern reveals itself in the form of fixed offset values in pixel readings, and it can be easily extracted when the sensor is not exposed to any light. However, the drawback of this approach is that today, cameras are designed to compensate for this type of an artifact. Later, Geradts *et al.* [13] proposed using sensor imperfections in the form of hot and dead pixels, pixel traps, and pixel defects in order to match images with cameras. Although their results show that these imperfections are unique to imaging sensors and they are quite robust to JPEG compression, most digital cameras, today deploy mechanisms to detect and compensate pixel imperfections through post-processing, which restricts the applicability of their technique.

Recently, similar to [14], Lukáš *et al.* [15] and Chen *et al.* [16], [17] proposed a more reliable sensor noise-based source digital camera and camcorder identification method. Their method is based on the extraction of the unique photoresponse nonuniformity (PRNU) noise pattern which is caused by the impurities in silicon wafers and sensor imperfections. These imperfections affect the light sensitivity of each individual pixel and cause a fixed noise pattern. Similarly, Khanna *et al.* [18], Gou *et al.* [12], and recently Gloe *et al.* [20] have extended PRNU noise extraction methodology to source scanner identification where the imaging sensor is typically a 1-D linear array. The drawback of this approach is that it is very hard to synchronize the scanner noise pattern with the noise residue extracted from the scanned image. This is due to difficulty in controlling the document position during scanning. Therefore, authors extracted statistical characteristics of PRNU noise and deployed machine learning methods to identify the scanner brand and model. It should be noted that utilizing feature-based classifiers makes these methods less effective in individual source scanner identification.

## II. SENSOR DUST CHARACTERISTICS

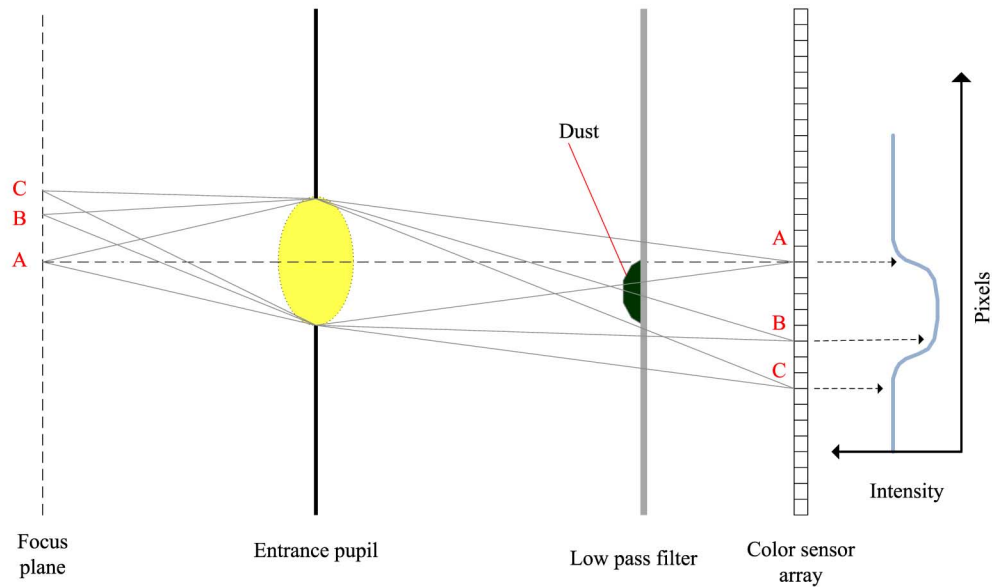
Essentially, dust spots are the shadows of the dust particles in front of the imaging sensor. The shape and darkness of the dust spots are determined primarily by the following factors: distance between the dust particle and imaging sensor, camera focal length, and size of aperture. A general optical model showing the formation of dust spots is given in Fig. 3. When the focal plane is illuminated uniformly, all imaging sensors will yield the same intensity values. However, in the presence of sensor dust, light beams interact with the dust particles and some of the light energy is absorbed by the dust particles. The amount of the absorbed energy is directly related to the parameter  $f$ -number ( $F/\#$ ) which is defined as the ratio between the focal length  $f$  and the aperture  $A$

$$f\text{-number} = \frac{f}{A}. \quad (1)$$

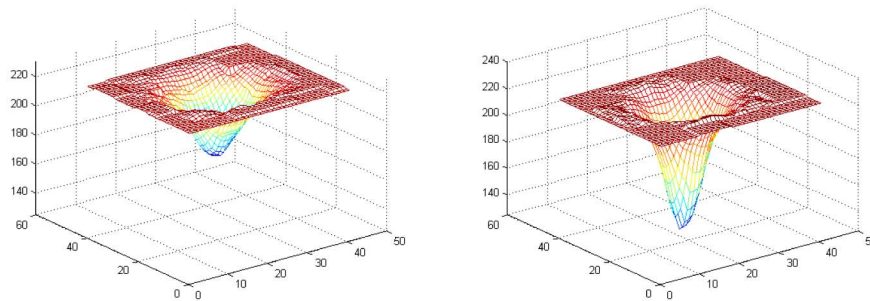
<sup>4</sup>[Online]. Available: [pixinfo.com/en/articles/ccd-dust-removal/](http://pixinfo.com/en/articles/ccd-dust-removal/).

<sup>5</sup>The reported dust removal performances defined based on a successfully cleaned number of initially present dust spots are as follows: Olympus E-300: 50%, Canon EOS-400D: 5%, Pentax K10D: 0%; and Sony Alpha A10: 0%.

<sup>6</sup>[Online]. Available: [www.usa.canon.com/consumer](http://www.usa.canon.com/consumer).



(a) Formation of dust spot under uniform illumination.



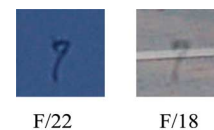
(b) Intensity degradation due to a dust speck (F/22). (c) Intensity degradation due to a dust speck (F/32).

Fig. 3. Intensity degradation due to the dust spot.

At small apertures and high  $f$ -numbers, the light source can be assumed to be a pinpoint source resulting in a relatively narrow light cone which can be blocked mostly with a tiny sensor dust. As a result, a strong dust shadow will appear on the image. This phenomenon is illustrated in Fig. 3(a). On the other hand, for wide apertures or small  $f$ -numbers which cause wide light cones in the DSLR body, most light beams pass around the dust spots causing a blurry and soft blemish in the image. In Fig. 3(b) and (c) and Fig. 6, the actual intensity degradations caused by dust spots are shown for different  $f$ -numbers. It can be seen from the figures that the change in  $f$ -number affects the intensity and radius of the dust spot wherein an increase in the  $f$ -number (smaller aperture) causes dust spots to appear darker and smaller.

#### A. Dust-Spot Shape

The dust particles in front of the imaging sensor mostly appear as round-shaped blemishes (see Figs. 1 and 2). However, dust spots with different shapes are also possible due to larger particles, such as lint or hair (Fig. 4). Since these large spots,

Fig. 4. Spot of hair/lint for different  $f$ -numbers (Nikon D50).

with unique shapes, are likely to cause very large intensity degradations, they are easily noticeable. Although this type of sensor dust is very suitable for camera identification, it is likely to attract the user's attention due to their annoying appearance. As a result, they are more likely to be cleaned out. Therefore, in this paper, we will focus on dust spots due to much smaller particles that yield round-shaped dust spots that are less likely to be cleaned by many users and are, in fact, difficult to clean as discussed earlier.

#### B. Dust-Spot Size

In this section, the formation of dust spots as a function of the camera parameters is analyzed. The optical dust-spot model,

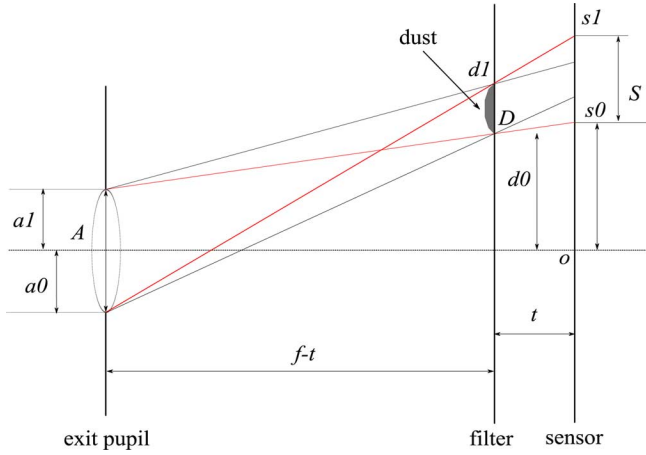
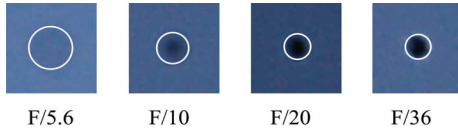


Fig. 5. Optical dust-spot model.

Fig. 6. Same dust spot for different  $f$ -numbers. The focal length is fixed to 55 mm (Nikon D50).

we assume, is depicted in Fig. 5, where the parameters  $A$ ,  $f$ ,  $t$ ,  $D$ , and  $S$  refer to the aperture, focal length, filter width, dust diameter, and dust shadow diameter, respectively. Assuming a circular dust spot, its size on the image can be computed. Let  $s_1$  and  $s_0$  points define the diameter of the dust shadow ( $S$ ) on the imaging sensor; and let  $d_1$  and  $d_0$  points define the diameter of the actual dust particle ( $D$ ). From the similarity of triangles,  $s_0$  and  $s_1$  can be written in terms of focal length, aperture, and the distance of dust particle ( $d_0$  and  $d_1$ ) to the image optical center  $o$  (see Fig. 5) as follows:

$$s_0 = \frac{f \cdot d_0 - t \cdot a_1}{f - t} \quad (2)$$

$$s_1 = \frac{f \cdot d_1 + t \cdot a_0}{f - t}. \quad (3)$$

Hence, the dust-spot (shadow) diameter  $S = s_1 - s_0$  on the imaging sensor becomes

$$S = D \frac{f}{f - t} + A \frac{t}{f - t}. \quad (4)$$

Essentially, (4) states that the size of the dust spot is directly proportional to the DSLR aperture  $A$ , which agrees with the observation in Fig. 6. Similarly, Table I and Fig. 7 show the change in diameter of a dust spot for fixed focal length and different apertures. It can also be seen from the table that the dust-spot size decreases with a decrease in aperture.

### C. Dust-Spot Movement

Although actual dust positions are stable on an imaging sensor, the positions of dust spots are affected by  $f$ -number changes. To see how a dust-spot position changes with aperture  $A$  and focal length  $f$ , a new variable ( $\rho = s_0 + s_1/2$ ) is defined

TABLE I  
DUST-SPOT PROPERTIES FOR DIFFERENT  $f$ -NUMBERS ( $f = 55$  mm, NIKON D50). IMAGE DIMENSIONS: 1504  $\times$  1000

F-number [F/#]	5.6	10	20	36
Aperture [mm]	9.82	5.5	2.75	1.53
Max. intensity degradation	11	46	61	83
Dust spot diameter [pixels]	20	14	11	10

which denotes the center of the dust shadow. To see how the dust shadow center is related to camera parameters,  $s_0$  and  $s_1$ , which are computed in (2) and (3), are substituted into the formula and  $\rho$  is obtained as

$$\rho = \frac{f(d_0 + d_1) + t(a_0 - a_1)}{2(f - t)} \quad (5)$$

$$\rho = \frac{d_0 + d_1}{2} \frac{f}{f - t} \quad (6)$$

where  $a_0$  and  $a_1$  define the aperture size. The equation shown before implies that the dust-spot position is not affected by the aperture but rather by the focal length. Indeed in Fig. 6, blemish center positions do not change with different apertures. However, the focal length can be changed with a zoom lens and different focal lengths may shift the dust spots.

Let us define the dust-spot shift  $\Delta\rho$  as the distance between dust-spot centers  $\Delta\rho = \rho_1 - \rho_0$ , where  $\rho_0$  and  $\rho_1$  are the dust-spot centers with focal length  $f_0$  and  $f_1$ , respectively. By substituting (6) into the definition, the dust-spot shift is obtained as

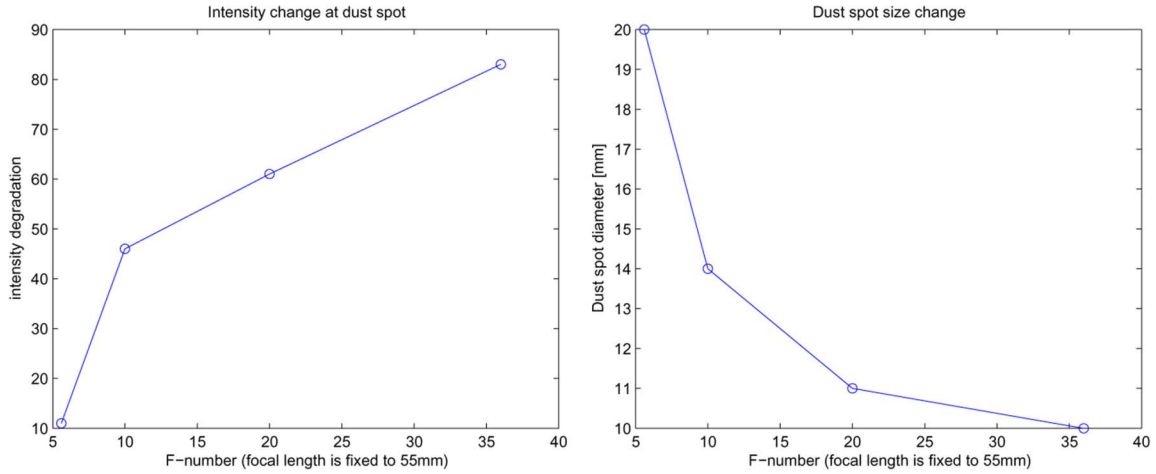
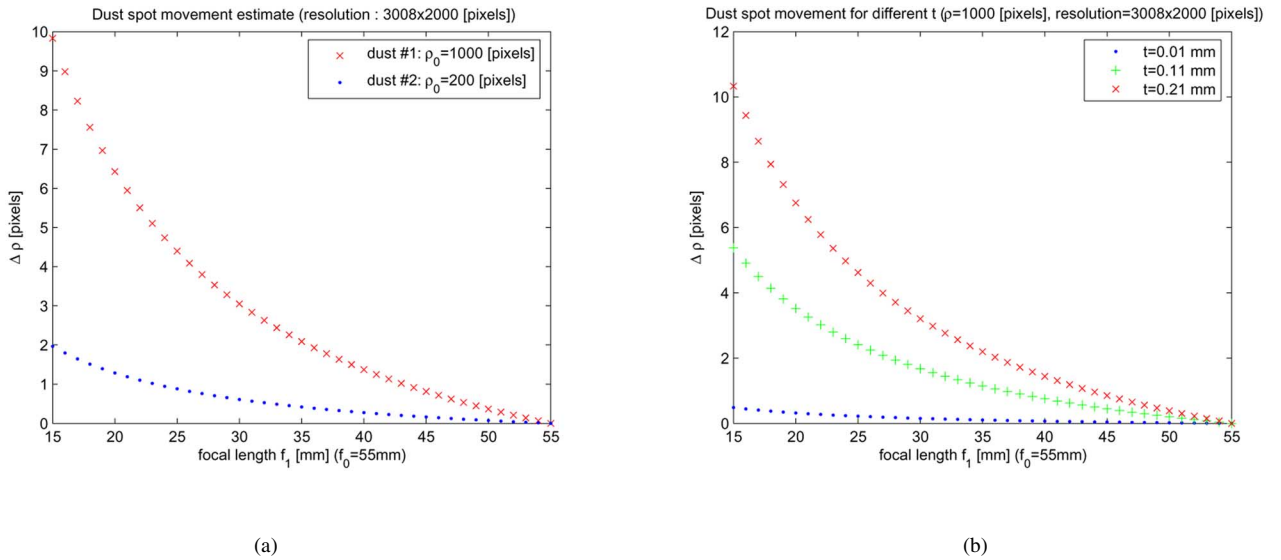
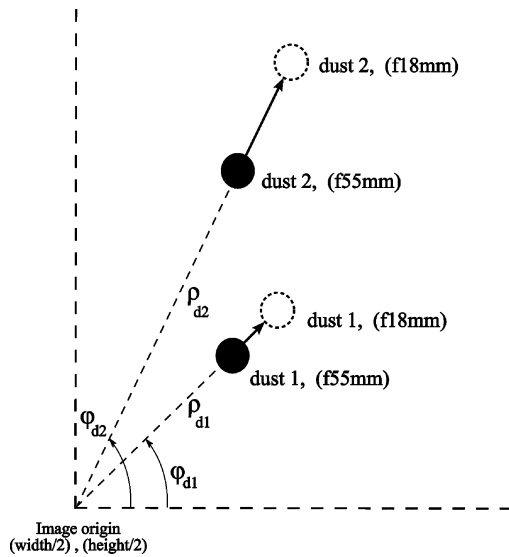
$$\Delta\rho = \frac{(f_0 - f_1)t}{(f_1 - t)(f_0 - t)} \frac{d_0 + d_1}{2} \quad (7)$$

$$\Delta\rho = \frac{f_0 - f_1}{f_0(f_1 - t)} \cdot t \cdot \rho_0. \quad (8)$$

It is seen from the equation that the dust-spot shift is directly proportional to the radial dust position and the filter width  $t$ . However, in (8) the relation between the focal length change ( $f_0 - f_1$ ) and the dust-spot shift is not clear. To visualize this relation, (8) was evaluated over a set of different focal length  $f_1$  and  $t$  values for a fixed  $f_0$  (55 mm). The evaluation results are depicted in Fig. 8.

It can be seen from Fig. 8 that the shift in a dust spot depends on the focal length change ( $f_0 - f_1$ ) reciprocally. Besides, the dust-spot shift magnitude is also determined by the actual dust position on the filter component. The farther the dust ( $d_0$ ) is from the image origin ( $o$ ), the higher the shift with the change in focal length is. Apparently, the shift vectors lie along the image radial axes. To measure the shift vectors from real images, we assume that the origin of the image is also the optical center of the image. In Fig. 9, the dust shift phenomenon is illustrated where a reduction in focal length causes dust spots in the image to move outward along the radial axis.

Experimental results for measuring dust-spot shifts are given in Table II and Fig. 10 for a Nikon D50 DSLR camera. In measuring the shifts, two different images (with 1504  $\times$  1000 resolution) were taken at two different focal lengths of 18 mm (F/18) and 55 mm (F/36). From these images, four distinct dust spots were determined. Their radial positions from the image center were measured in polar coordinates. The radial shift magnitudes

Fig. 7. Dust-spot properties for different  $f$ -numbers.Fig. 8. Dust-spot movement analysis based on the proposed optical model. (a) Radial shifts of two dust spots.  $t$  and  $f_0$  are fixed.  $f_1$  is changed. (b) Dust-spot shifts for different  $t$  values.Fig. 9. Dust-spot shifts due to focal length  $f$  change.TABLE II  
DUST-SPOT POSITIONS AND SHIFTS FOR DIFFERENT FOCAL LENGTHS (NIKON D50)

	2nd position $f=18\text{mm}$		1st position $f=55\text{mm}$		Shifts	
	$\rho$ [pixels]	$\varphi$ [deg.]	$\rho$ [pixels]	$\varphi$ [deg.]	$\Delta\rho$	$\Delta\varphi$
1	392.8	80.5	389.9	80.5	3.0	0.1
2	457.0	72.4	451.3	72.5	5.7	-0.2
3	626.6	50.5	617.2	50.4	9.4	0.1
4	830.0	147.7	817.7	147.7	12.2	-0.0

( $\rho$ ) and angles ( $\varphi$ ) are given in the last columns for four different dust spots. It is seen from the table that the results are consistent with (8). From (8), it is possible to estimate the shift magnitudes. Since the  $t$  parameter of Nikon D50 is not known, first,  $t$  was estimated from the observed dust shifts in Table II as 0.35 mm by the least square method. Then, for each dust spot in the table, the shift magnitudes were estimated from (8) with 1.2 pixel mean absolute error. The estimation results are given with the actual values in Fig. 10.

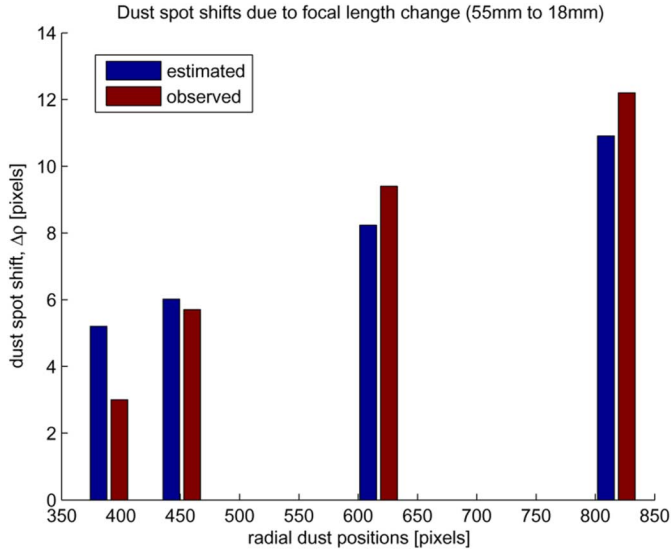


Fig. 10. Estimated and observed dust-spot shifts for different focal lengths and positions.

### III. FORENSICS USE OF SENSOR DUST

In this section, we develop a technique for camera identification based on sensor dust detection. The use of dust spots for source camera identification first requires determining the positions of dust spots in an image. Since dust particles do not tend to move easily, they appear in all images taken with high  $F$ -numbers, and their proper cleaning is not trivial, these dust-spot locations can be used as a unique fingerprint of a DSLR camera. This fingerprint can be represented by a camera dust template that includes information on all detectable dust spots. It must be noted that this template can be directly obtained from images taken by the camera at a high  $f$ -number setting or from a number of images when the camera is not available by collating dust spots detected from different images together. To decide whether an image is taken by a given DSLR, the dust spots detected in an image can be compared to those in the camera dust template and a decision is made depending on the match between detected dust spots and the template. It should be noted that the lack of a match does not allow a conclusive decision since dust specks might have been cleaned manually after the capture of the image with cloning tools.

#### A. Dust-Spot Detection

In recent years, several software-based dust-spot detection and removal schemes have been proposed [21]–[24]. These methods usually aim at detecting dust positions from a flat background by examining intensity gradient degradations. However, our experimental studies show that gradient-based approaches suffer from relatively high false detection rates due to their sensitivity to intensity variations. Alternatively, in this paper, and based on our earlier work [19], we propose a model-based dust detection scheme that utilizes dust-spot intensity and shape characteristics in detecting dust spots. In our proposed detection scheme, we model dust spots based on their two major characteristics: 1) an abrupt change on image

intensity surface as a function of the  $f$ -number and 2) they appear mostly in the form of rounded shapes.

As mentioned before, sensor dust can be viewed as black, out-of-focus spots with a soft intensity transition. Our observations of various actual dust spots also confirm that they have Gaussian-like intensity degradations. This phenomenon can be viewed in Fig. 3(b) and (c). Inspired from these figures and many other examples, we utilize a Gaussian intensity loss model (i.e., a 2-D Gaussian function to model dust spots). Our model for the dust spot is expressed as follows:

$$\text{intensity loss}(x, y) = \frac{-G}{\sqrt{2\pi\sigma^2}} \cdot e^{-(x-w)^2+(y-w)^2/2\sigma^2}$$

$$x, y = 0, \dots, 2w \quad (9)$$

where  $G$ ,  $\sigma$ , and  $2w$  are the gain factor, standard deviation, and template width, respectively.

Essentially, dust-spot dimensions depend on the  $f$ -number and dust size directly [see (4)]. To capture this relation in our model,  $\sigma$  is selected to adjust the size of the dust-spot model. The intensity loss of the model is controlled by the parameter  $G$ . Although, for a given image, the  $f$ -number can be obtained from the EXIF data, the actual dust size cannot be known. Nevertheless, to investigate the more general case, we do not utilize the EXIF header information for this purpose. Hence, the model parameter  $\sigma$  that determines the dust-spot size needs to be estimated blindly.

In detecting dust spots in an image, we correlate the Gaussian dust model with the image for various  $\sigma$  values (9) over all pixel positions via fast normalized cross-correlation (NCC) [25]. This results in a 2-D map of values where each value is computed by cross-correlating the Gaussian dust model with a window of size  $2w \times 2w$  sliding over the image, which will be referred to as NCC output.

In the NCC output, values higher than an empirically set threshold are selected as potential dust-spot candidates. To reduce the search range of the parameter  $\sigma$  and to speed up the detection process, all images are suitably downsampled to a midresolution ( $800 \times 533$ ) while preserving their aspect ratio. In addition, to further simplify the processing, images are converted to gray level while still preserving intensity degradations due to dust spots.

In Table III, the largest dust-spot dimensions observed in seven different cameras with various  $f$ -numbers are given. All dust dimensions were measured after downsampling (to  $800 \times 533$  pixels resolution). Although the information in Table III is not sufficient to represent dust-size distribution, it can be used in selecting a range for  $\sigma$  values.

Our measurements in Table III indicate that dust spots generally have an area that is less than that of a window of  $10 \times 10$  pixels. Based on this observation, we chose  $\sigma = 1$  or  $\sigma = 2$  which correspond to small ( $6 \times 6$  pixels) and large ( $12 \times 12$  pixels) dust spots, respectively.

To exemplify the relation between the NCC output and model parameter  $\sigma$ , our dust detection scheme was applied to various dust spots. In Table IV, NCC local maxima values computed through our detection scheme for different dust spots taken from various DSLR cameras ( $2 \times 2$  pixels to  $20 \times 20$  pixels) are given. As seen from the table, the corresponding NCC local

TABLE III  
MAX. DETECTED DUST-SPOT SIZE FOR DIFFERENT  
DSLR CAMERAS (IMAGE SIZES:  $800 \times 533$ )

DSLR camera	Max. dust spot size [pixels]	f-number
Sigma SD10	3×3	11
Sigma SD9	5×7	5.6
Nikon D1	7×7	N/A
Nikon D50	8×8	10
Nikon D70	7×7	N/A
Canon EOS Rebel	7×8	22
Canon EOS Rebel XTi	9×9	13

TABLE IV  
MAX. NORM. CROSS-CORRELATION (NCC) OUTPUTS  
FOR VARIOUS DUST-SPOT (IMAGE SIZES:  $800 \times 533$ )

Dust no	Dust spot size [pixels]	Max depth	Max NCC ( $G=5, 2w=20+3\sigma$ )
1	2×2	13	0.71 ( $\sigma = 1$ )
2	6×6	33	0.81 ( $\sigma = 1$ )
3	14×14	9	0.53 ( $\sigma = 2$ )
4	20×20	11	0.44 ( $\sigma = 2$ )



Dust spot depth: 42

Dust spot size: 4x4 [pixels]

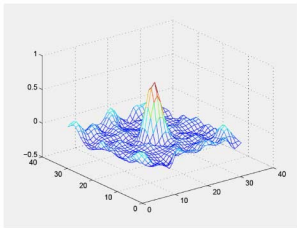
(a) small spot



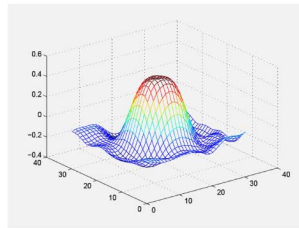
Dust spot depth: 6

Dust spot size: 13x13 [pixels]

(b) large spot



(c) small spot, max NCC=0.81,  $\sigma = 1$



(d) large spot, max NCC=0.53,  $\sigma = 2$

Fig. 11. Normalized cross-correlation (NCC) outputs for different dust spots.  $4 \times 4$  [pixels] dust (left),  $13 \times 13$  [pixels] dust (right).

maxima of dust spots takes values between 0.44 and 0.81 which are sufficiently high for dust-spot detection. To visualize the spatial NCC output variations, NCC mesh plots of two different dust spots are given in Fig. 11. In the figure, our dust model produces Gaussian-like NCC outputs with high NCC values at the center of dust spots (0.81 for small dust and 0.53 for a relatively large one). In the camera identification phase, the proposed dust-spot detection scheme is repeated for each  $\sigma$  value (i.e.,  $\sigma = 1, 2$ ). Then, all detected dust-spot positions are combined together to detect various-sized dust spots in a given image.

Obviously, the described template matching-based method is likely to detect some content-dependent intensity degradations as dust spots. To reduce content-dependent false detections, template matching is applied only in low and medium detail image regions determined through measurement of intensity gradients. Further, the following steps are performed to reduce false detections.

1) *Binary Map Analysis*: For a given image, NCC values are computed for each Gaussian dust model corresponding to different  $\sigma$  values. Then, a binary dust template is generated by thresholding the correlation values such that values smaller than a preset value are set to zero and others to one. In the binary dust map, each binary object, obtained by combining together neighboring binary components, is indexed and a list of dust-spot candidates is formed. We then exploit the fact that most dust spots have rounded shapes. This is realized by computing the area of each binary object and removing the extremely large or line-shaped objects, resulting in edges and textures from the binary dust map.

2) *Validation of Correlation Results*: After binary map analysis, all detected dust spots are re-evaluated by analyzing the values in the NCC output. For actual dust spots, NCC values are expected to monotonically decrease around the center of the dust spot (see Figs. 11 and 18). For this, several NCC values around each binary object are checked along a circular path to ensure that NCC values exhibit such a decrease. The binary objects that do not confirm to this observation are also removed from the binary dust map.

3) *Spatial Analysis*: The spatial intensity loss characteristics of each dust-spot candidate (e.g., remaining binary objects in the binary dust map) is examined by constructing a contour map of a region surrounding each candidate dust spot and counting the number of local minima. If there is a global minimum in the selected region, the corresponding binary object is tagged as dust. On the other hand, the presence of the multiple local minima implies that detected dust-spot candidates are most likely the result of image content and, therefore, corresponding binary objects are removed in the final binary dust map.

## B. Camera Dust Template Generation

Due to difficulties in dust detection, template generation can be a challenging task. For instance, differentiating the slight intensity variations due to sensor dust in highly textured regions from the image content is not trivial. Similarly, at large apertures, most dust spots become almost invisible without significant intensity degradation. However, in cases where the camera is available, these problems can be easily circumvented as the user can adjust the camera settings to make the dust spots visible as much as possible. (This can be achieved by taking a bright and unfocused sky photograph with the highest  $f$ -number setting.) This would make almost every dust in the camera appear as black, tiny spots on a flat background. In such a case, even one image is sufficient to create a quite reliable camera dust template.

On the other hand, if the DSLR camera is not accessible but only a set of images taken with the source camera in question are available, the camera template can be estimated by combining all detected dust spots from all images in the set. To create a camera dust template, the dust detection procedure is applied to all available images that are known to be taken with the same DSLR camera. Since these images may be taken with different  $f$ -lengths, detected positions for dust spots may not overlay with each other, see (8). This misalignment is due to different  $f$ -number values. To be able to deal with the shifts in dust spots, in creating the binary map, we allow each dust

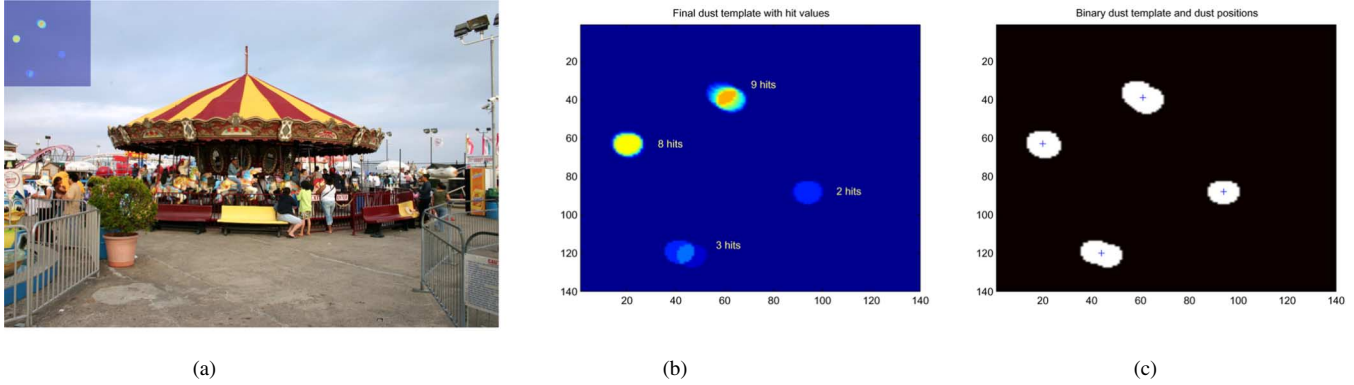


Fig. 12. Dust template generation from a set of images (Canon EOS Digital Rebel). (a) Image used to create the dust template. (b) Upper left portion of the dust template. Its actual size is shown at the left. (c) Binary version of the dust template.

candidate position to occupy a circle rather than assigning fixed coordinates.

As can be seen in (8), the dust-spot shift magnitude is directly proportional to the filter width  $t$ . This entails that the largest radial shift may vary among DSLR cameras with different brands/models. Hence, in generating the template, the radius of the binary circle is determined empirically by measuring the largest radial shifts of dust spots in several images of different DSLR cameras. At the end, all binary dust maps are simply added up to create the final camera dust template.

To exemplify camera dust template generation, ten images taken with different  $f$ -numbers were used. The DSLR camera used in this experiment was a Canon EOS Digital Rebel. In all images, dust spots were determined and all results were combined to create the camera dust template. To eliminate the false detections in the template, we utilized a threshold. If a dust spot appears in only one image and does not appear in other images used in template generation, that spot is removed from the dust template.

The upper left part of the final dust template obtained is shown in Fig. 12. In Fig. 12(a), the number of coinciding dust spots is given. The hot colors refer to high number of dust matches. In the figure, the dust shifts due to different focal lengths can be seen clearly. In Fig. 12(b), the binary version of the final dust template is given. Final dust positions were computed as centroid points of each dust region in the binary map. These points are represented with the “+” symbol in Fig. 12(b).

After template generation, all dust spots in the dust template are tagged with different numbers. Dust centroid positions and the number of coinciding dust in that positions are saved in a file to be used in camera identification. It is assumed that the higher the number of coinciding dust spots is, the more dominant the corresponding dust spot will be. Therefore, those dust spots will be given more weight in making a decision. In addition, all dust positions detected in each individual image are also maintained since the camera dust template contains only averaged dust locations. This information could not be used in detecting the dust-spot shifts properly since we lose individual dust positions for different  $f$ -numbers after computing centroid positions in a binary dust template [see Fig. 12(b)].

### C. Camera Identification

The final step of DSLR camera identification is done by matching the dust spots detected in an image with dust spots in the camera dust template. The identification process is comprised of three steps:

- Step 1) dust-spot detection and matching;
- Step 2) computing a confidence value for each matching dust spot;
- Step 3) decision making.

In the first step, dust spots are detected as explained in Section III-A. Once dust spots are located, each dust position is matched with the dust positions in the camera dust template. The comparison is realized by measuring Euclidian distances. If the distance is lower than a predetermined value, the corresponding dust position is added to the matching dust-spot list.

In the second step, three metrics are computed for each of the matching dust spots as follows.

- 1) The dust occurrence metric  $m_1$  is the number of coinciding dust for the corresponding dust spot in the dust template. Higher values of  $m_1$  correspond to salient dust spots.
- 2) Smoothness metric  $m_2$  presents the smoothness of the region in which a dust spot was detected. Measuring the amount of local intensity variations is essential in making decisions since dust-spot detection in smooth regions is more reliable than in busy regions. This is computed via the intensity gradient around the dust spot as a binary value. For a smooth region,  $m_2$  becomes one, and for a nonflat or nonsmooth region around the dust spot, it becomes zero.
- 3) Shift validity metric  $m_3$  indicates the validity of a dust spot based on the shift it exhibits. To compute  $m_3$ , we do the following.
  - Each dust spot in the matched dust-spot list is tracked in all template images, used in template generation. (It should be noted a different subset of dust spots will be detected in each image.)
  - For each dust spot in the list, a set of the shift vectors (i.e., magnitude and angle) is computed by measuring the shifts between a dust spot and its matched counterparts in the template images).

- Shift vectors associated with each of the template images are collected together.

The underlying idea is that since the template images and the image in question are likely to be taken at different  $f$ -numbers, the relative shift between the dust spots in the image and any of the template images should be consistent. (Fig. 12 displays part of a camera dust template and its binary version. Since each template image is captured under a different  $f$ -number, the detected dust spots appear shifted and, as a result, they do not align in the template.) In other words, each shift vector along the radial axis should be in the same direction (i.e., all shifts should be either towards or outwards from the optical center). (Note that we assume the image center is the optical center.) If a measured shift vector is significantly away from the radial axis, that dust spot is ignored and not used for source matching. Similarly, for a given dust spot, if a significant shift magnitude is not measured,  $m_3$  is assigned a zero value; otherwise,  $m_3 = 1$ .

Essentially, the higher the aforementioned three metrics are, the more likely that dust detection is correct. If a dust spot is detected in a smooth region,  $m_2$  becomes one. For that dust spot, if the shift is valid,  $m_3$  becomes one too. Finally, if the detected dust spot corresponds to a region where a dominant dust spot lies where many dust spots coincide,  $m_1$  takes as value the number of coinciding dust spots in the template. To bound  $m_1$  between zero and one, as  $m_2$  and  $m_3$ , it is applied to a monotonically increasing function  $f$  whose upper bound is one. In this work, we used Gauss error function as the normalization function. For perfect dust detection, the sum of  $m_1$ ,  $m_2$ , and normalized  $m_3$  metrics becomes three for one dust spot.

In the third step, the three metrics computed for each dust spot are then combined to determine an overall confidence in identification of the source DSLR. Finally, to make a decision, the statistic  $C$  is obtained by summing up the confidence score of all dust spots as

$$C = \sum_{i=1}^N f\left(\frac{m_1(i)}{\alpha}\right) + m_2(i) + m_3(i) \cdot u(N-2) \quad (10)$$

$$u(x) = \begin{cases} 0, & x < 0 \\ 1, & x \geq 0 \end{cases} \quad (11)$$

where  $N$  is the number of detected dust spots in a given image,  $f$  is a monotonically increasing normalization function which takes values between 0 and 1,  $\alpha$  is a scaling factor, and  $u$  is a step function defined in (11), respectively. (We select  $f$  to be the Gauss error function, but any monotonically increasing bounded function can be alternatively used.) The reason we used a step function in (10) is to validate the dust shift direction based on the availability of at least two dust spots. If two or more dust spots shift consistently, we infer that dust-spot candidates are not false positives. To make a decision, we apply a threshold to the confidence value. The images which yield the confidence values above the detection threshold are assumed to be taken with the DSLR camera from which the dust template is generated. On the other hand, low confidence values do not imply that they are not taken with the suspected DSLR.

TABLE V  
CAMERA DUST TEMPLATE GENERATION

Num. of template images	Number of dusts in the dust template		
	5 images	10 images	15 images
Sky not visible	2	3	15
Sky visible	33	47	55

TABLE VI  
EFFECT OF THE VARIATION IN THE DUST  
TEMPLATE TO IDENTIFICATION ACCURACY

Num. of template images	TP and FP rates (threshold=1.7)		
	5 images	10 images	15 images
Sky not visible	TP:38/100	TP:38/100	TP:74/100
	FP:1/500	FP:1/500	FP:1/500
Sky visible	TP:86/100	TP:90/100	TP:94/100
	FP:1/500	FP:3/500	FP:5/500

#### IV. EXPERIMENTS

To test the efficacy of proposed scheme, several experiments were performed with various DSLR cameras and image sets. Before starting the experimental analysis, we compute the upperbound on false dust detection probability. Let  $M$  be the amount of dust in a camera dust template and all dust spots be represented with circles of radius  $R$  in the template. We assume here that all dust spots are uniformly distributed in the template. When one pixel position in an image is randomly picked, the probability of that the pixel not coinciding with any of dust spots in the template can be computed as

$$P_{\text{nomatch}} = 1 - \frac{M\pi R^2}{W \cdot H} \quad (12)$$

where  $W$  and  $H$  are the image dimensions. Hence, when  $N$  pixel positions are chosen randomly from the image, the probability of at least one of them coinciding with a dust spot becomes

$$P_{\text{match}} = 1 - (P_{\text{nomatch}})^N. \quad (13)$$

For  $M = 15$ ,  $N = 5$ ,  $R = 8$ ,  $W = 800$ ,  $H = 533$ ,  $P_{\text{match}}$  becomes 0.0349. It should be noted by requiring a greater number of random matches (as opposed at least 1), this figure can be further reduced. In addition, dust-spot shape characteristics and shift analysis make it possible to reduce the false detection rate to lower values.

##### A. Effect of Image Content on Dust Template

Creating an accurate and error-free camera dust template is very essential for the identification step. If the camera itself is available, the detection of dust spots and dust template generation is very straightforward. By adjusting the focal length to its maximum value, almost all dust spots can become visible and easily detectable. However, in the absence of the camera, dust template generation is highly affected by the content of the images used in template generation. Intuitively, images with large and smooth regions would yield more accurate dust template than images with busy content.

To determine this, we conducted an experiment with 110 images downloaded from the web.<sup>7</sup> From the EXIF image headers, it was deduced that the images were taken with a Sigma SD9

<sup>7</sup>[Online]. Available: [www.pbase.com/chucklantz/](http://www.pbase.com/chucklantz/).

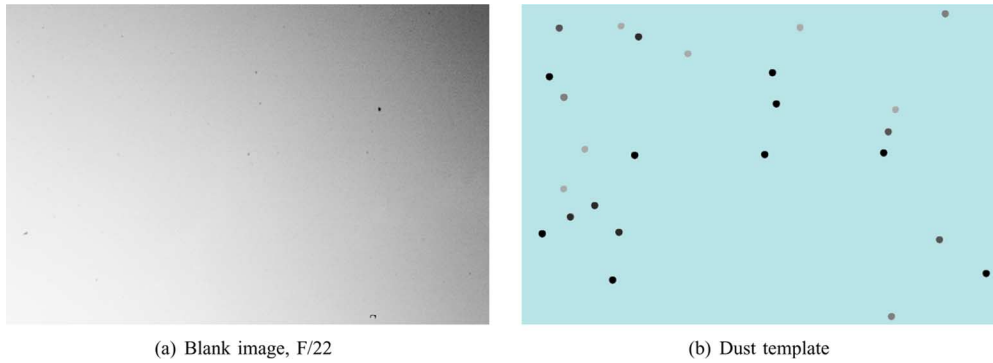


Fig. 13. Canon EOS dust template created with three blank images with different  $f$ -numbers (F/13, F/22, F36).

DSLR camera (will be referred as Camera 3). Out of 110 images, two different image sets were created. The first set consisted of 15 images in which there was no apparent sky or extensive flat region, and the second set consisted of 15 images in which the sky was clearly visible. For each image set, three dust templates were generated from 5, 10, and 15 images, as described in Section III-B. The amount of dust in each dust template is given in Table V. Not surprisingly, the greatest number of dust spots is achieved for 15 images with flat regions. To test the detection performances of these six templates, the proposed camera identification scheme was tested using the rest of the 100 images and 500 images taken with different DSLR and compact cameras. The true-positive (TP) and false-positive (FP) rates for six different dust templates are given in Table VI. In the table, the TP rate significantly increases as the amount of dust in the template increases with a small increase in FP (see Tables V and VI).

It is seen from Table VI that high detection accuracy is possible even with the five images used in template generation with smooth content. Nevertheless, to achieve such high accuracy with the images that do not contain any visible sky, the number of images used in template generation should be as high as possible.

### B. Case-I: Source Camera Available

In this section, we assume that the DSLR source device is available at hand. In experiments, we used Nikon D-50 and Canon EOS Digital Rebel cameras with 18–55 mm lenses. To introduce dust into the cameras, camera lenses were detached while the cameras were powered up several times in an environment where tiny particles, such as lint, hair, and dust, were present.

Then, the camera dust templates of Nikon and Canon DSLR cameras were created by capturing three flat background photographs at three different  $f$ -numbers (i.e., F/13, F/22, and F/36). The template of the Canon DSLR is depicted in Fig. 13 along with one of the images used in template generation. In Fig. 13(b), the detected dust spots in the template are shown as gray spots where the degree of darkness of the dust spots represents the number of hits ( $m_2$ ) in the dust template which was obtained as described in Section III-B. In Fig. 13(b), a line-shaped lint particle is also detected as its size is very close to that of dust spots.

To test source camera identification performance, 100 images were taken in different environments with different  $f$ -numbers with each Canon and Nikon DSLR camera. To estimate the FP rate, 1000 images were taken with eight different digital cameras (including Canon A80, Canon Rebel XT, Dimage Z3, Canon S2 IS, Cybershot, DSC-P72, DSC-S90, and EX-Z850). Then, the source camera identification procedure was performed on these 100+1000 images for both Canon and Nikon dust templates. The identification confidence values for all 1100 images are given in Fig. 14 where the  $x$ -axis represents image indices and the  $y$ -axis represents the overall confidence values defined in (10). In the figures, the dot symbol corresponds to previously unseen images taken by the source DSLR camera. The dust templates for Canon and Nikon DSLR cameras are comprised of 38 and 36 dust spots, respectively. The decision threshold (threshold = 1.7) is set to fix FP probability at 0.002. The corresponding TP rate and accuracy, where accuracy is defined as the ratio of all true detections to number of images, were computed as 0.610 and 0.963 for Nikon, and 0.920 and 0.991 for Canon DSLR cameras. The TP rate for Nikon was significantly smaller than the Canon image set due to the fact that the Nikon set contained so many nonsmooth and complex images which made the decision more prone to error.

### C. Case-II: Source Camera Unavailable

In this case, ten images taken with Nikon and Canon DSLR cameras were used to create the camera dust template and then the camera identification procedure was applied. In generating the camera dust template, images, which consist of mostly flat regions, were used. Then, the camera identification scheme was applied to the same image sets which consist of 100 + 1000 images. The detection accuracy results obtained using dust templates created from ten images with large smooth regions are given in Fig. 15.

Due to the problem of creating an accurate dust template from a set of images, taken with uncontrolled conditions, with busy contents, the amount of dust in the dust templates decreased to 4 from 36 for Nikon, and 10 from 38 for Canon, respectively. Since confidence metric increases with the number of dust spots (10), in Fig. 15, the range of confidence values decreases. The small number of dust spots in the template makes it possible to achieve very low FP rates, with lower detection threshold. Thus, the detection threshold was reset for the unavailable camera case

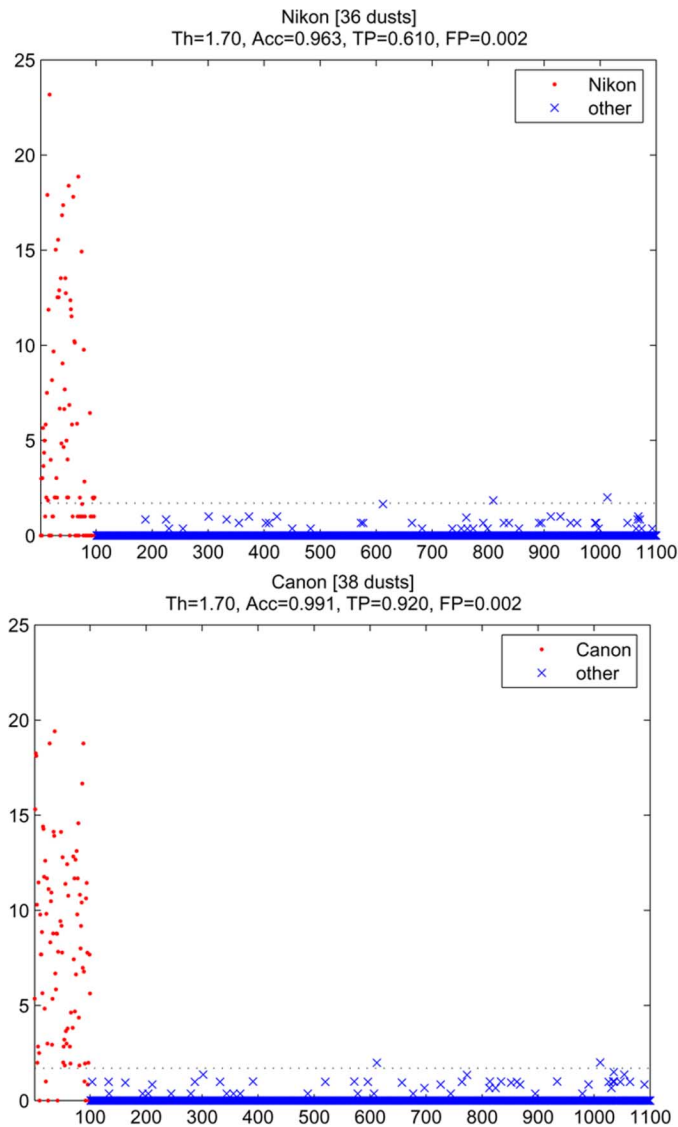


Fig. 14. Camera identification results (camera available).

(threshold = 1.05). For this new setting, the detection accuracy for Nikon D50 decreased from 0.963 (TP = 0.610, FP = 0.002) to 0.951 (TP = 0.460, FP = 0.000). For Canon DSLR, the detection accuracy decreased from 0.991 (TP = 0.920, FP = 0.002) to 0.985 (TP = 0.840, FP = 0.000) (see Figs. 14 and 15). Although there is a small decrease in detection accuracy for the Nikon and Canon cameras, the FP rate is reduced to zero despite a lower threshold value.

To make a more realistic experiment, the aforementioned experiment was repeated using the image set (110 images of camera 3) obtained from the web.<sup>8</sup> Selecting the ten images with the largest flat regions, the dust template of the DSLR Sigma SD9 camera was obtained. The dust template and sample images used in template generation are depicted in Fig. 16. In the template, there are 29 dust spots. The sky images in the image set make it possible to reliably detect many dust locations even though the actual camera is not available. The generated dust template is tested on the rest of 100 images and

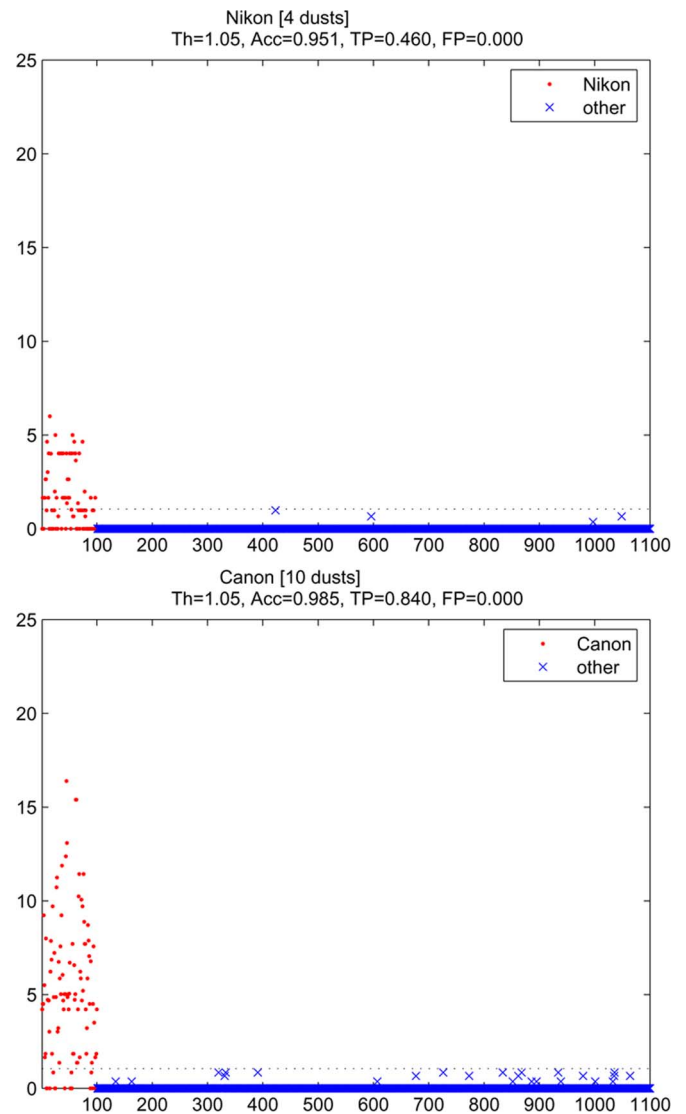


Fig. 15. Camera identification results (camera not available).

1000 images from other digital cameras. The identification performance for this image set is given in Fig. 17. It can be seen from the figure that individual camera identification can be accomplished with 0.991 accuracy, 0.001 FP, and 0.910 TP rates for the given image sets for the same threshold (threshold = 1.05).

#### D. Robustness

We evaluated the performance of the dust detection scheme and source identification accuracy under two common types of processing.

1) *Downsizing*: Since most dust spots appear with significant intensity degradations affecting a large group of pixels, they are not strongly affected from image resizing. To determine the impact of downsizing on detection accuracy, 100 images of Canon EOS were downsized 50%. Then, the scheme was applied to original and downsized image sets. For the original Canon image set, 89 out of 100 images were detected correctly. This rate becomes 88 out of 100 for a 50% downsized image set. It should be noted that in the camera identification scheme, all

<sup>8</sup>[Online]. Available: [www.pbase.com/chucklantz/](http://www.pbase.com/chucklantz/).

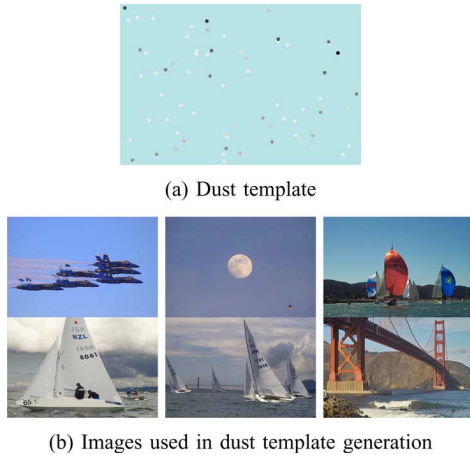


Fig. 16. Dust template of camera 3 and the images (downloaded from the Internet) used in template generation.

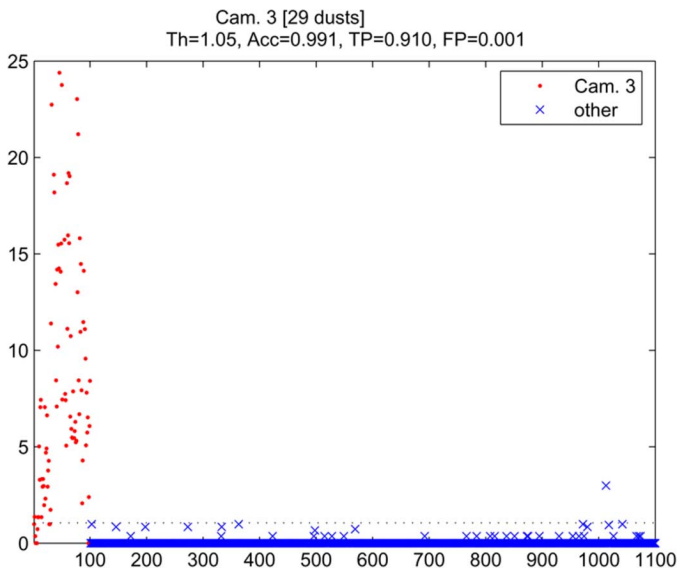


Fig. 17. Identification results for 100 images downloaded from the Internet (camera 3).

input images were resized to  $800 \times 533$  resolution regardless of input resolution.

2) *JPEG Compression*: To analyze the impact of compression on the performance of source identification accuracy, 100 images both from Nikon and Canon image sets and 500 images from other digital cameras were compressed at JPEG quality 50. The identification results are given in Table VII from which it can be seen that the proposed scheme is viable even under strong JPEG compression. In the table, solely one Nikon image is identified better under JPEG compression. The NCC output for original and compressed versions of that image is given in Fig. 18. In the figure, it is seen that the JPEG compression increases the number of local maxima exceeding the detection threshold in the NCC output. As a result, a dust spot which is not visible in NCC output, corresponding to the original image, becomes detectable after JPEG compression. However, at the same time, the number of false detections has also increased significantly.

TABLE VII  
ROBUSTNESS TO JPEG COMPRESSION

Camera	Original		JPEG Q50	
	TP	FP	TP	FP
Nikon	61/100	0/500	62/100	2/500
Canon	92/100	0/500	91/100	1/500

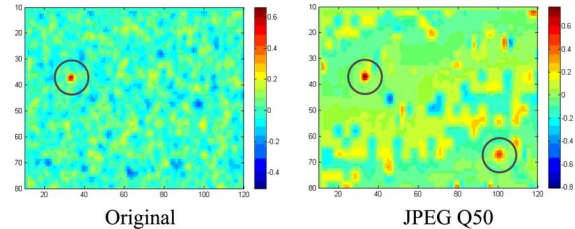


Fig. 18. Effect of JPEG compression on dust-spot detection. The images are the outputs of NNC.

The red points in the right figure show the falsely detected dust spots as a result of JPEG compression.

The proposed identification scheme can be improved by representing dust positions as nodes in a specific graph. This extension could make the proposed scheme more robust to geometric/desynchronization attacks. However, for now, we leave this extension as a future work.

## V. CONCLUSION

In this paper, we have introduced a new source DSLR camera identification scheme based on sensor dust traces. The location and shape of dust specks in front of the imaging sensor and their persistence make dust spots a useful fingerprint for DSLR cameras. Although many DSLR cameras come with built-in dust removal mechanisms, these hardware-based removal solutions are not as effective as they claim to be. Besides, since most dust spots are not visible or visibly irritating, most DSLR users ignore them completely. To the our best knowledge, this is the first work in the literature which uses sensor dust spots for individual camera identification. The efficacy of the proposed camera identification scheme is tested on higher than 1000 images from different cameras. Experimental results show that the proposed scheme provides high detection accuracy with very low false alarm rates. Our experimental tests also show that the proposed scheme is quite robust to JPEG compression and downsizing. The biggest challenge in this research direction is the detection of dust spots in very complex regions and low  $f$ -numbers.

## ACKNOWLEDGMENT

The authors would like to thank M. Pollitt at the University of Central Florida for suggesting this line of research.

## REFERENCES

- [1] D. L. M. Sacchi, F. Agnoli, and E. F. Loftus, "Changing history: Doctorated photographs affect memory for past public events," *Appl. Cognit. Psychol.*, vol. 21, no. 8, pp. 1005–1022, Nov. 2007.
- [2] H. Farid, *Deception: Methods, Motives, Contexts and Consequences*. Stanford, CA: Stanford Univ. Press, 2007, ch. Digital Doctoring: Can we trust photographs?.

- [3] H. T. Sencar and N. Memon, "Overview of state-of-the-art in digital image forensics," in *Indian Statistical Institute Platinum Jubilee Monograph series titled Statistical Science and Interdisciplinary Research*. Singapore: World Scientific, 2008.
- [4] T. V. Lanh, K.-S. Chong, S. Emmanuel, and M. S. Kankanhalli, "A survey on digital camera image forensic methods," in *Proc. IEEE Int. Conf. Multimedia Expo.*, 2007, pp. 16–19.
- [5] T.-T. Ng, S.-F. Chang, C.-Y. Lin, and Q. Sun, "Passive-blind image forensics," in *Multimedia Security Technologies for Digital Rights*, W. Zeng, H. Yu, and A. C. Lin, Eds. New York: Elsevier, 2006.
- [6] G. Friedman, "The trustworthy digital camera: Restoring credibility to the photographic image," *IEEE Trans. Consum. Electron.*, vol. 39, no. 4, pp. 905–910, Nov. 1993.
- [7] P. Blythe and J. Fridrich, "Secure digital camera," in *Proc. Digital Forensic Research Workshop*, Aug. 2004, pp. 11–13.
- [8] M. Kharrazi, H. T. Sencar, and N. Memon, "Blind source camera identification," in *Proc. IEEE Int. Conf. Image Processing*, Oct. 2004, vol. 1, pp. 709–712.
- [9] A. Swaminathan, M. Wu, and K. J. R. Liu, "Non intrusive forensic analysis of visual sensors using output images," *IEEE Trans. Inf. Forensics Security*, vol. 2, no. 1, pp. 91–106, Mar. 2007.
- [10] Y. Long and Y. Huang, "Image based source camera identification using demosaicking," in *Proc. IEEE 8th Workshop Multimedia Signal Processing*, Victoria, BC, Canada, Oct. 2006, pp. 4190–424.
- [11] K. S. Choi, E. Y. Lam, and K. K. Y. Wong, "Source camera identification using footprints from lens aberration," *Proc. SPIE Digital Photography II*, vol. 6069, pp. 172–179, Feb. 2006.
- [12] H. Gou, A. Swaminathan, and M. Wu, "Robust scanner identification based on noise features," *Proc. SPIE Security, Steganography, Watermarking of Multimedia Contents IX*, vol. 6505, p. 65050, Feb. 2007.
- [13] Z. J. Geradts, J. Bijhold, M. Kieft, K. Kurosawa, K. Kuroki, and N. Saitoh, "Methods for identification of images acquired with digital cameras," *Proc. SPIE Enabling Technologies for Law Enforcement and Security*, vol. 4232, pp. 505–512, Feb. 2001.
- [14] K. Kurosawa, K. Kuroki, and N. Saitoh, "Ccd Fingerprint method—Identification of a video camera from videotaped images," in *Proc. ICIP*, Kobe, Japan, 1999, pp. 537–540.
- [15] J. Lukáš, J. Fridrich, and M. Goljan, "Digital camera identification from sensor noise," *IEEE Trans. Inf. Forensics Security*, vol. 1, no. 2, pp. 205–214, Jun. 2006.
- [16] M. Chen, J. Fridrich, and M. Goljan, "Digital imaging sensor identification (further study)," *Proc. SPIE Security, Steganography, Watermarking of Multimedia Contents IX*, vol. 6505, p. 65050, Feb. 2007.
- [17] M. Chen, J. Fridrich, M. Goljan, and J. Lukáš, "Source digital camcorder identification using sensor photo response non-uniformity," *Proc. SPIE Security, Steganography, Watermarking of Multimedia Contents IX*, vol. 6505, p. 65051, 2007.
- [18] N. Khanna, A. K. Mikkilineni, G. T. C. Chiu, J. P. Allebach, and E. J. Delp, "Scanner identification using sensor pattern noise," *Proc. SPIE Security, Steganography, Watermarking of Multimedia Contents IX*, vol. 6505, p. 65051, Feb. 2007.
- [19] A. E. Dirik, T. H. Sencar, and M. Nasir, "Source camera identification based on sensor dust characteristics," in *Proc. IEEE Workshop Signal Processing Applications for Public Security and Forensics*, Apr. 2007, pp. 1–6.
- [20] T. Gloe, E. Franz, and A. Winkler, E. J. Delp III and P. W. Wah, Eds., "Forensics for flatbed scanners," in *Proc. Security, Steganography, and Watermarking of Multimedia Contents IX*, Feb. 2007, vol. 6505, p. 65051.
- [21] A. Krainiok and R. T. Minner, "Method and system for detecting and tagging dust and scratches in a digital image," U.S. Patent 6 233 364 B1, May 2001.
- [22] E. Steinberg, Y. Prilutsky, and P. Corcoran, "Method of detecting and correcting dust in digital images based on aura and shadow region analysis," pub. A1, Mar. 2005.
- [23] A. Zamfir, A. Drimborean, M. Zamfir, V. Buzuloiu, E. Steinberg, and D. Ursu, "An optical model of the appearance of blemishes in digital photographs," *Proc. SPIE, Digital Photography III*, vol. 6502, pp. 011–0112, Feb. 2007.
- [24] E. Steinberg, P. Bigioi, and A. Zamfir, "Detection and removal of blemishes in digital images utilizing original images of defocused scenes," pub. A1, May 2007.
- [25] J. Lewis, "Fast normalized cross-correlation," *Proc. Vision Interface*, pp. 120–123, 1995.



**Ahmet Emir Dirik** received the B.S. and M.S. degrees in electrical engineering from Uludag University, Bursa, Turkey, and is currently pursuing the Ph.D. degree in signal processing at the Department of Electrical and Computer Engineering at the Polytechnic University, Brooklyn, NY.

His research interests include multimedia forensics, information security, and data hiding.



**Husrev Taha Sencar** received the Ph.D. degree in electrical engineering from the New Jersey Institute of Technology, Newark, in 2004.

Currently, he is a Postdoctoral Researcher with the Information Systems and Internet Security Laboratory of the Polytechnic University, Brooklyn, NY. His research interests are the security of multimedia and communications.



**Nasir Memon** is a Professor in the Computer Science Department at the Polytechnic University, Brooklyn, NY.

He is the Director of the Information Systems and Internet Security (ISIS) Lab at Polytechnic University. His research interests include data compression, computer and network security, digital forensics, and multimedia data security.